CANCER

Sight and switch off: Nerve density visualization for interventions targeting nerves in prostate cancer

Huijuan You[1,2]*, Wenting Shang[2]*†, Xiangde Min[1], Jeffrey Weinreb[3], Qiubai Li[4], Michael Leapman[5], Liang Wang[1]†, Jie Tian[2,6]†

Copyright © 2020 The Authors, some rights reserved; exclusive licensee American Association for the Advancement of Science. No claim to original U.S. Government Works. Distributed under a Creative Commons Attribution NonCommercial License 4.0 (CC BY-NC).

Nerve density is associated with prostate cancer (PCa) aggressiveness and prognosis. Thus far, no visualization methods have been developed to assess nerve density of PCa in vivo. We compounded propranolol-conjugated superparamagnetic iron oxide nerve peptide nanoparticles (PSN NPs), which achieved the nerve density visualization of PCa with high sensitivity and high specificity, and facilitated assessment of nerve density and aggressiveness of PCa using magnetic resonance imaging and magnetic particle imaging. Moreover, PSN NPs facilitated targeted therapy for PCa. PSN NPs increased the survival rate of mice with orthotopic PCa to 83.3% and decreased nerve densities and proliferation indexes by more than twofold compared with the control groups. The present study, thus, developed a technology to visualize the nerve density of PCa and facilitate targeted neural drug delivery to tumors to efficiently inhibit PCa progression. Our study provides a potential basis for clinical imaging and therapeutic interventions targeting nerves in PCa.

INTRODUCTION

Recent studies have reported that innervation of prostate cancer (PCa) favors tumor progression (*1*–*6*). The sympathetic (adrenergic) and parasympathetic (cholinergic) nervous systems play notable roles in PCa development and invasion, respectively (schematic S1). Symbiotic interactions between PCa and nerves result in costimulation of growth (*7*). An analysis of samples derived from patients with PCa revealed a higher nerve density among patients with high-risk PCa, and a high nerve density is associated with an increased tumor proliferative index and poor survival (*1*). Current clinical treatments for PCa include surgery, androgen deprivation therapy (ADT), radiation therapy (RT), ablation, chemotherapy, etc. (*8*, *9*). These treatments do not appear to precisely attenuate the effect of nerves on the tumor, which potentially maintain PCa progression in some patients. Thus far, no effective visualization method for assessing nerve density of PCa has been developed. These limitations potentially deter the complete treatment of PCa with high nerve density; however, PCa patients with low nerve density are subsequently at a risk of overtreatment. Hence, it is critical to develop a visualization method to assess the nerve density of PCa in vivo.

Magnetic resonance imaging (MRI) is the best noninvasive method to clinically diagnose PCa (*8*). Superparamagnetic iron oxide (SPIO) nanoparticles (NPs) have been used as contrast-enhancing agents for clinical MRI for more than 20 years (*10*–*15*). Recent studies have reported that SPIO NPs can also be used for magnetic particle imaging (MPI) (*16*–*20*), an emerging imaging technology, and can effectively reduce background noise from the tissue specimen while assuring high sensitivity and in-depth penetration (*21*–*26*). A combination of MRI and MPI involving SPIO NPs would corroborate the benefits of both methods through functional complementation, thus improving imaging quality. Such a combinatorial method may improve the sensitivity of visualization of the nerve density of PCa.

To accurately assess the nerve density of PCa, a method to improve the specificity of visualization of nerve density is urgently required. Nerve-binding peptide, NP41, detected using a phage display method (*27*), preferentially binds to neural laminins in the extracellular matrix (*28*). NP41 has been used to highlight autonomic nerves within the prostate (*29*), facial nerves (*30*, *31*), vagal nerves of the esophagus and stomach (*32*), and degenerated nerves (*28*). Since PCa is innervated, NP41, with increased specificity, is potentially applicable for visualizing nerve abundance in PCa.

In this study, we developed a highly sensitive and specific nanoprobe to visualize the nerve density of PCa, which can precisely distinguish between the high and low nerve density of PCa. Furthermore, numerous studies have reported that patients with PCa receiving neural drugs (β-blockers) are at a decreased risk of recurrence and mortality (*33*–*35*). Thus, the drug-loading properties of the nanoprobe (*36*, *37*) were harnessed to load a neural drug serving as a nerve blocker in PCa, thus facilitating interventions in PCa with high nerve density and improving nanoprobe effectiveness and usability. Together, we exploited a nanoprobe that enabled not only visualization of nerve density but also targeting delivery of neural drug to inhibit tumor progression.

RESULTS

NP41 facilitated nerve targeting in orthotopic PCa

The potential of NP41 in visualizing the nerve density of PCa was verified through multiple methods. A mouse model of orthotopic PCa was generated to mimic the natural PCa microenvironment. Nerves were identified in orthotopic PCa 11 weeks after inoculation of PC-3luc cells into the ventral prostate of BALb/c nude male mice (Fig. 1A). Neural identity was verified through tyrosine hydroxylase (TH) staining in adrenergic varicose fibers, vesicular acetylcholine transporter (VAChT) staining in cholinergic nerve fibers, and

[1]Department of Radiology, Tongji Hospital, Tongji Medical College, Huazhong University of Science and Technology, Wuhan, Hubei 430030, China. [2]CAS Key Laboratory of Molecular Imaging, Institute of Automation, Chinese Academy of Sciences, Beijing 100190, China. [3]Department of Radiology and Biomedical Imaging, Yale University School of Medicine, New Haven, CT 208042, USA. [4]Department of Radiology, UT Southwestern Medical Center, 5323 Harry Hines Blvd., Dallas, TX 75390, USA. [5]Department of Urology, Yale University School of Medicine, New Haven, CT208042, USA. [6]Beijing Advanced Innovation Center for Big Data-Based Precision Medicine, School of Medicine, Beihang University, Beijing 100191, China.
*These authors contributed equally to this work.
†Corresponding author. Email: wenting.shang@ia.ac.cn (W.S.); wang6@tjh.tjmu.edu.cn (L.W.); jie.tian@ia.ac.cn (J.T.)

Downloaded from https://www.science.org on September 09, 2022

neurofilament heavy and light (NF-H/L) staining in neuron-specific cytoskeletal subunits (Fig. 1A). Western blot analysis was performed to compare expression levels of NP41-binding targets (neural laminins) (*28*) in PCa tissues and healthy prostate tissues. Consequently, neural laminins were up-regulated in PCa tissues in comparison with healthy prostate tissues (Fig. 1B and fig. S1).

Since optical imaging is highly sensitive (*38*), we used a small-molecule nanoprobe, Cy7 (cyanine 7)–NP41, as a standard reference (*39*), to verify in vivo and in vitro binding of NP41 with the nerves of orthotopic PCa. Cy7-NP41 was characterized. The qualitative and quantitative analyses of the fluorescence intensity of Cy7-NP41 indicated an optimal concentration of 40 μM Cy7-NP41 for fluorescence imaging (FLI) (fig. S2, A and B). Mass spectroscopic analysis revealed that Cy7–NHS (*N*-hydroxysuccinimide) and NP41 were stably conjugated (fig. S2C). The absorption peak (fig. S2D), fluorescence excitation and emission spectra (fig. S2, E and F), and serum stability

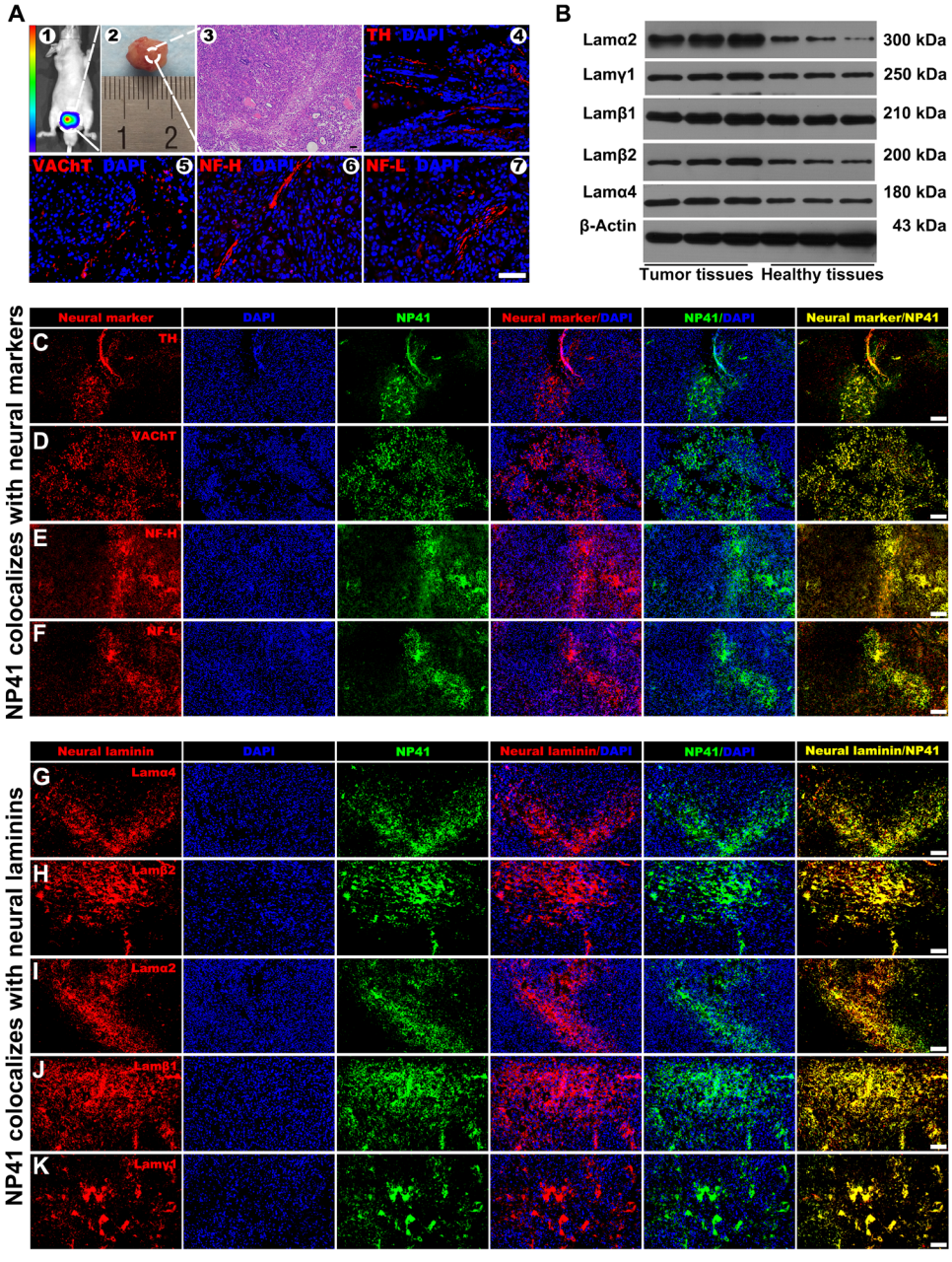

Fig. 1. The nerve-binding peptide, NP41, can target cancer-related nerves of PCa. (**A**) Representative in vivo BLI of BALb/c nude male mice 11 weeks after injection of PC-3luc cells into the ventral prostate (1) and image of the orthotopic prostate tumor (2). Representative H&E staining of orthotopic prostate tumor (3). Neural identity was confirmed by immunofluorescence staining of TH (4), VAChT (5), NF-H (6) and NF-L (7). DAPI (4′,6-diamidino-2-phenylindole), blue; TH, VACHT, NF-H, and NF-L, red. Scale bar, 50 μm. (**B**) Western blot of the expression of neural laminins in prostate tumor tissues and healthy prostate tissues. (**C** to **F**) Immunofluorescence staining of TH (C), VAChT (D), NF-H (E), and NF-L (F) colocalizes with NP41 binding, respectively. Scale bars, 100 μm. (**G** to **K**) Immunofluorescence staining of laminin-α4 (Lamα4, G), laminin-β2 (Lamβ2, H), laminin-α2 (Lamα2, I), laminin-β1 (Lamβ1, J), and laminin-γ1 (Lamγ1, K) colocalizes with NP41 binding, respectively. Scale bars, 100 μm.

Downloaded from https://www.science.org on September 09, 2022

(fig. S2G) reflected excellent optical performance of Cy7-NP41. No distinct cytotoxicity was observed in PC-3luc cells and DU-145luc cells (fig. S2H), indicating the superiority of Cy7-NP41 for further experiments. Optical imaging of nerves of orthotopic PCa was performed in vivo and in vitro using Cy7-NP41.

NP41 targeting was verified in vivo. Nerves in orthotopic PCa were marked with Cy7-NP41, but not with Cy7 alone (fig. S3A). Three-dimensional (3D) FLI and bioluminescence imaging (BLI) of Cy7-NP41 confirmed the presence of fluorescence signals in PCa in situ (fig. S3B). Cy7-NP41 gradually accumulated temporally in the tumor area and peaked 8 hours after injection, and the maximum tumor/normal tissue ratio (TNR) value was 6.1 ± 0.28, being threefold that of free Cy7 (2.2 ± 0.13) (fig. S3C). Representative FLI revealed the orthotopic PCa in vivo and the corresponding exposed tumor tissue (fig. S3D). Tumors and major organs harvested 48 hours after injection further better elucidated the accumulation of Cy7-NP41 at the tumor site than free Cy7 and indicated the target specificity of NP41 (fig. S3, E and F). Cy7-NP41, rather than free Cy7, bound to the abundant nerves in the tumor area, thereby enabling nerve visualization. These results show the corresponding distribution of nerve density in tumor tissues (fig. S3G), suggesting the potential of NP41 to detect nerves in PCa.

Furthermore, NP41 targeting was verified in vitro. NP41 localized similarly in PCa tissue sections fluorescently stained not only for TH, VAChT, NF-H, and NF-L (Fig. 1, C to F) but also for neural laminins (Fig. 1, G to K), suggesting that NP41 can target nerves in PCa with high specificity, revealing its potential in visualizing tumor innervation in PCa.

Visualization of nerve density with high sensitivity and specificity

We successfully synthesized a nanoprobe to visualize the nerve density of PCa and intervene in nerves in PCa. The generation of propranolol-loaded SPIO-NP41 NPs (PSN NPs) is shown in Fig. 2A. We used various methods to accurately verify the synthesized nanoprobe (*40*). PSN NPs generated herein indeed exhibited high monodispersity and homogeneity, with average diameters of 10 ± 0.4 nm and hydrated particle size of 23 ± 6 nm, as revealed via transmission electron microscopy (TEM) (Fig. 2B) and dynamic light scattering (DLS) (Fig. 2C), respectively. TEM images revealed no distinct morphological changes in the propranolol-loaded SPIO NPs (PS NPs) before labeling with NP41 and PSN NPs after labeling with NP41 (Fig. 2B). Hydrated particle size, zeta potential, and ultraviolet-visible (UV-vis) absorption spectra were recorded to verify successful nanoprobe conjugation with NP41. The hydrated particle size and zeta potential of the PSN NPs were altered after labeling with NP41 (Fig. 2, C and D). The peptides on PSN NPs were evaluated using a UV-vis spectrophotometer. UV-vis absorption spectra revealed an 87% labeling efficiency with NP41 among PSN NPs (Fig. 2E and table S1). The magnetic signal of PSN NPs is an important property for in vivo detection. Hence, we used MRI and MPI to qualitatively verify the magnetic signals of PSN NPs under different concentrations. T2 relaxation times and MPI signals were concentration dependent. T2 relaxation times decreased, MPI signals were enhanced with an increase in PSN NPs levels (Fig. 2, F and H), and these magnetic signals were quantified. The relaxivity coefficients (R_2) values and MPI signals of PSN NPs were linearly correlated with PSN NPs concentrations (Fig. 2, G and I). The hysteresis loop revealed that PSN NPs yielded particularly highly saturated magnetization of 78 emu/g, thus displaying the superparamagnetic behavior of PSN NPs (Fig. 2J), further highlighting the potential applications of PSN NPs in MRI and MPI. The drug-loading content of PSN NPs was 0.82 mg/ml, as revealed through high-performance liquid chromatography (HPLC). At the 24th hour, the propranolol released from PSN NPs was 60.1% at pH 6.0 and 26.6% at pH 7.4 on HPLC (Fig. 2K). The time and pH dependence of propranolol release from PSN NPs suggest that an acidic tumor microenvironment (*41*) can promote the release of propranolol from PSN NPs. These results suggest the therapeutic potential of PSN NPs in PCa.

The effectiveness of the successfully synthesized nanoprobe was analyzed in vivo. We intravenously administered PS NPs and PSN NPs to mice via the tail vein and monitored their distribution at different time points (Fig. 3A). Before systemic administration of both NPs, the morphology and signal intensity of PCa were similar among both groups (Fig. 3A). However, 6 hours after PSN NPs administration, signal intensity on T2-weighted imaging (T2WI) of orthotopic PCa was decreased, which increased with time. Remarkable reductions in signal intensity were detected on T2WI in the tumor area 24 hours after PSN NPs administration (Fig. 3C). PSN NPs did not highlight the entire tumor, indicating that PSN NPs specifically bound to the nerves associated with PCa progression, thus enabling their visualization. However, these results were not obtained upon PS NPs administration. PS NPs are larger than 6 nm and are metabolized by the liver, intestine, and spleen and do not penetrate the tumor microenvironment (*42*); however, PSN NPs actively targeted abundant nerves in the PCa tissue. To further assess differences between the two groups via MRI, we performed quantitative analyses by calculating the TNR of the average signal intensity on MRI (Fig. 3C). The TNR of the PSN NPs was minimum at 24 hours after administration, yielding a significant difference between the PS NPs and PSN NPs groups. Therefore, the optimal time point to visualize the accumulation of PSN NPs in the tumor area was 24 hours after administration. Similarly, the difference in TNR between the PSN NPs and PS NPs groups was significant at 48 hours after administration.

Furthermore, MPI signal intensity for nerves at the tumor site was significantly greater upon administration of PSN NPs rather than PS NPs (Fig. 3, B and D). To visualize the distribution of PSN NPs and PS NPs, we acquired specimens from tumor tissue and major organs including the liver, spleen, and kidney for nuclear fast red and Prussian blue double staining. The accumulation of PSN NPs is greater than that of PS NPs in PCa owing to the target specificity of PSN NPs (Fig. 3E), again indicating toward the target specificity of NP41. Furthermore, the two groups of nanoprobes were taken up differently by the liver and spleen. Thus, PSN NPs facilitate highly sensitive and specific visualization of the nerve density of PCa in vivo.

PSN NPs facilitated distinguishing between the high and low nerve density of PCa

To determine whether PSN NPs distinguish between the high and low nerve density of PCa, we used two different methods, drug-based and surgical, to generate mice models of high and low nerve density orthotopic PCa.

The drug-based method involved the use of phosphate-buffered saline (PBS) and neurotoxic drug 6-hydroxydopamine (6OHDA), respectively (*43*). The nerve density of PCa was restrained owing to 6OHDA-mediated selective destruction of adrenergic neurons, thereby affecting orthotopic PCa progression (fig. S4A). On the

Downloaded from https://www.science.org on September 09, 2022

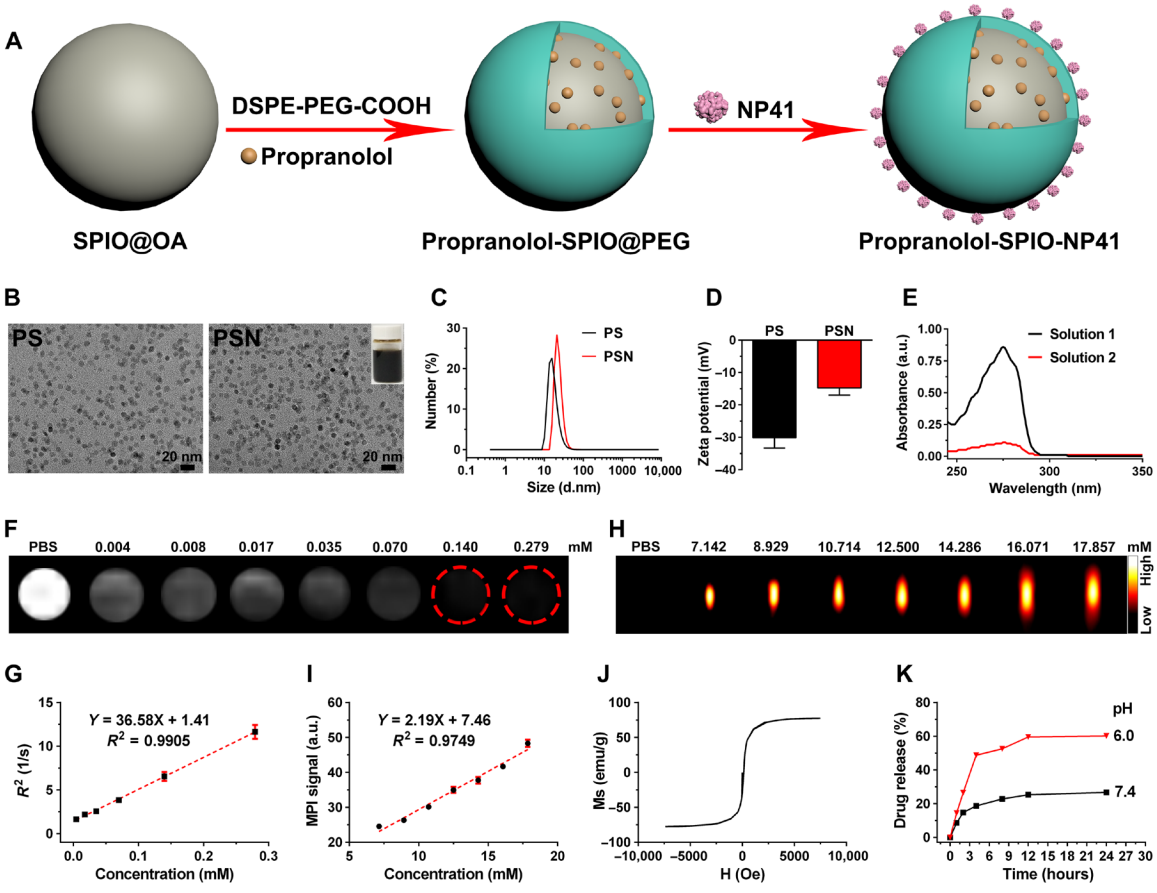

Fig. 2. Preparation and characterization of PSN NPs. (**A**) Schematic of the fabrication process. (**B**) TEM images of PS NPs before labeling with NP41 (left), and PSN NPs after labeling with NP41 (right). Inset shows the appearance of PSN NPs solution. (**C**) Hydrated particle size of PS NPs and PSN NPs. (**D**) Zeta potential of PS NPs and PSN NPs. (**E**) UV-vis absorption spectra of solutions 1 and 2. Solution 1: Peptide solution before PS NPs labeling with peptides. Solution 2: Supernatants isolated after PS NPs labeling with peptides. a.u., arbitrary units. (**F**) T_2-weighted MRI images and (**G**) T_2 relaxation rate of PSN NPs at various concentrations. The red dashed circles show the black MRI images as the PSN NPs concentration increased. (**H**) MPI images and (**I**) MPI signal of PSN NPs at various concentrations. (**J**) Room temperature magnetization curve of PSN NPs. (**K**) HPLC analysis of in vitro propranolol release profiles from PSN NPs in buffer at pH 6.0 and 7.4.

contrary, PBS did not affect neurogenesis in PCa and resulted in high-nerve-density orthotopic PCa (fig. S4B). Meanwhile, the proliferation (Ki-67) index was lower in 6OHDA-treated mice than in PBS-treated mice (fig. S4C).

The MRI and MPI signals of PBS-treated mice were remarkable at 24 hours after systemic administration of PSN NPs but not in 6OHDA-treated mice (Fig. 4, A and B). Significant differences were observed between the TNR (Fig. 4C) and MPI signal intensities (Fig. 4D) between PBS-treated mice and 6OHDA-treated mice. These results suggest that PSN NPs facilitate distinguishing of nerve densities on MRI and MPI. Prussian blue staining revealed that the PSN NPs accumulation was greater in PBS-treated than in 6OHDA-treated mice (Fig. 4E). Prussian blue and immunofluorescence staining suggested that PSN NPs accumulation was consistent with nerve density (Fig. 4, E and F). The MRI and MPI signals of PBS- and 6OHDA-treated mice corresponded with nerve density (Fig. 4F) and Ki-67 index (Fig. 4G). We analyzed the association between MRI and MPI signal intensities and pathological indexes including nerve density and Ki-67 index in PBS- and 6OHDA-treated mice. MRI revealed a lower TNR accompanied by a higher nerve density upon staining for TH, VAChT, NF-H, and NF-L in PBS-treated mice and a higher TNR accompanied by a lower nerve density upon staining for TH, VAChT, NF-H, and NF-L in 6OHDA-treated mice, thus revealing four significant negative correlations of TNR with TH ($P = 0.0113$, $R = -0.7110$, Spearman's correlation coefficients), VAChT ($P = 0.0124$, $R = -0.7040$), NF-H ($P = 0.0024$, $R = -0.8021$), and NF-L ($P = 0.0026$, $R = -0.7986$) (Fig. 4H). Furthermore, MPI revealed a higher signal intensity accompanied by a higher nerve density upon TH, VAChT, NF-H, and NF-L staining in PBS-treated mice and a lower signal intensity accompanied by a lower nerve density upon TH, VAChT, NF-H, and NF-L staining in 6OHDA-treated mice, thus revealing significant positive correlations of MPI signal intensity with nerve density (TH: $P = 0.0033$, $R = 0.7902$; VAChT: $P = 0.0078$, $R = 0.7413$; NF-H: $P = 0.0062$, $R = 0.7552$; NF-L: $P = 0.0004$, $R = 0.8741$; Fig. 4I). Moreover, similar to nerve density, Ki-67 index in PBS- and 6OHDA-treated mice was associated with TNR ($P = 0.0157$, $R = -0.6865$; Fig. 4H) and MPI signal intensity ($P = 0.0055$, $R = 0.7622$; Fig. 4I), indicating that PCa with a higher Ki-67 index displayed high-intensity signals on MRI and MPI. Nerve density upon TH, VAChT, NF-H, and NF-L staining was positively correlated with the Ki-67 index in PBS- and 6OHDA-treated mice (Fig. 4J), concurrent with previous reports (*1*). These

Downloaded from https://www.science.org on September 09, 2022

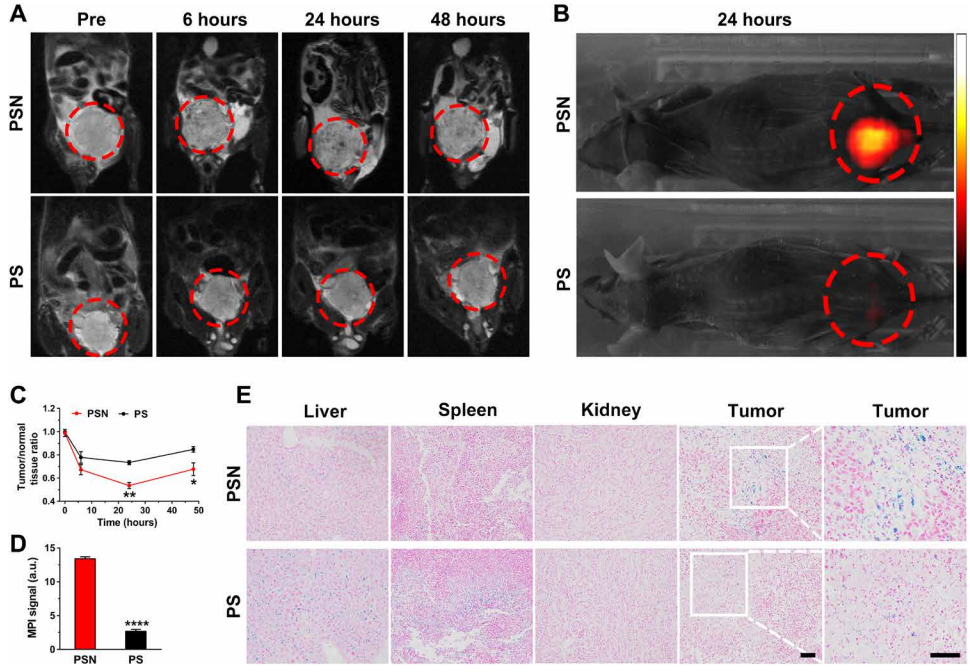

Fig. 3. Imaging difference of PSN NPs and PS NPs. (**A**) T_2-weighted MRI images of nerve density of PCa acquired at different time points before and after systemic administration of PSN NPs and PS NPs, respectively. The red dashed circles indicate the nerve density of PCa in situ. (**B**) MPI images of nerve density of PCa obtained 24 hours following systemic injection of PSN NPs and PS NPs. (**C**) Quantification of TNR in the PSN NPs and PS NPs groups at corresponding time points to (A). TNR values show notable difference at 24 and 48 hours after injection of two nanoprobes ($P = 0.021$ and $P = 0.046$, respectively). (**D**) Quantification of MPI signal in the PSN NPs and PS NPs groups at corresponding time point to (B). MPI signal values display notable difference at 24 hours after injection of PSN NPs and PS NPs ($P < 0.0001$). (**E**) Nuclear fast red and Prussian blue double staining images of major organs (liver, spleen, and kidney) and tumor after intravenous administration of PSN NPs and PS NPs. *$P < 0.05$, **$P < 0.01$, and ****$P < 0.0001$, Student's t test. Scale bars, 50 μm. Error bars represent SEM.

results indicate that visualization of nerve density is a potential novel approach to predict nerve density and aggressiveness of PCa in vivo.

FLI was performed to confirm whether NP41 can distinguish high and low nerve density in PBS- and 6OHDA-treated mice with PCa. Unlike 6OHDA-treated mice, the fluorescence signals of PBS-treated mice remarkably localized to the tumor region, as revealed through BLI (fig. S5A). Although the localization of the fluorescence signal of 6OHDA-treated mice was consistent with the findings of BLI, the fluorescence intensity was markedly low (fig. S5A), and the difference in fluorescence intensity between PBS- and 6OHDA-treated mice was significant (fig. S5D). The fluorescence intensity on FLI and BLI between PBS- and 6OHDA-treated mice corresponded to the nerve density and Ki-67 index (fig. S5, B and C). We analyzed the association of fluorescence intensity in PBS- and 6OHDA-treated mice with the nerve density and Ki-67 index in PCa. Significant positive correlations were observed between fluorescence intensity and TH, NF-H, and NF-L, as well as Ki-67 index (fig. S5, E, G, H, and I). Fluorescence intensity was not associated with nerve density on VAChT staining ($P = 0.0633$, $R = 0.5569$; fig. S5F). Hence, it is necessary to generate a PCa model that more realistically simulates the neural microenvironment of PCa to confirm whether PSN NPs can distinguish the high and low nerve density of PCa.

To further determine whether PSN NPs distinguish the distribution of nerve density of PCa, we next constructed mouse models of high- and low-nerve-density orthotopic PCa in mice with sham-operated nerve-intact and surgically severed afferent hypogastric nerves (HGNx), respectively. Surgical denervation inhibited PCa progression in comparison with sham-operated nerve-intact mice (fig. S6A). Quantitative analysis of pathological results revealed that the high- and low-nerve-density orthotopic PCa model was successfully generated (fig. S6, B and C).

After administration of PSN NPs, qualitative and quantitative analyses of MRI (Fig. 5, A and C) and MPI signal intensities (Fig. 5, B and D) between sham-operated nerve-intact mice and surgically severed HGNx mice yielded consistent results with the results obtained through drug treatment. Prussian blue staining (Fig. 5E), nerve densities (Fig. 5F), and Ki-67 indexes (Fig. 5G) displayed similar trends upon surgery and drug treatment. We analyzed the association of MRI and MPI signal intensities with nerve density and Ki-67 indexes in sham-operated nerve-intact and surgically severed HGNx mice. Significant negative correlations of TNR with nerve density and Ki-67 index (TH: $P = 0.0070$, $R = -0.7483$; VAChT: $P = 0.0001$, $R = -0.9091$; NF-H: $P = 0.0022$, $R = -0.8112$; NF-L: $P = 0.0019$, $R = -0.8182$; Ki-67 index: $P = 0.0014$, $R = -0.8266$; Fig. 5H) were observed, consistent with the results obtained upon drug treatment. Furthermore, significant positive correlations of MPI signal intensity with nerve density and Ki-67 index (TH: $P = 0.0008$, $R = 0.8531$; VAChT: $P = 0.0278$, $R = 0.6434$; NF-H: $P = 0.0170$, $R = 0.6853$; NF-L: $P = 0.0062$, $R = 0.7552$; Ki-67 index: $P < 0.0001$, $R = 0.9422$; Fig. 5I) were observed, consistent with the results obtained upon drug treatment. Nerve density upon TH, VAChT, NF-H, and NF-L staining was positively correlated with the Ki-67 index in sham-operated nerve-intact and surgically severed HGNx mice (Fig. 5J), concurrent with previous reports (*1*). These results further suggest that the visualization and assessment of nerve density is a potentially effective method of predicting PCa aggressiveness.

Downloaded from https://www.science.org on September 09, 2022

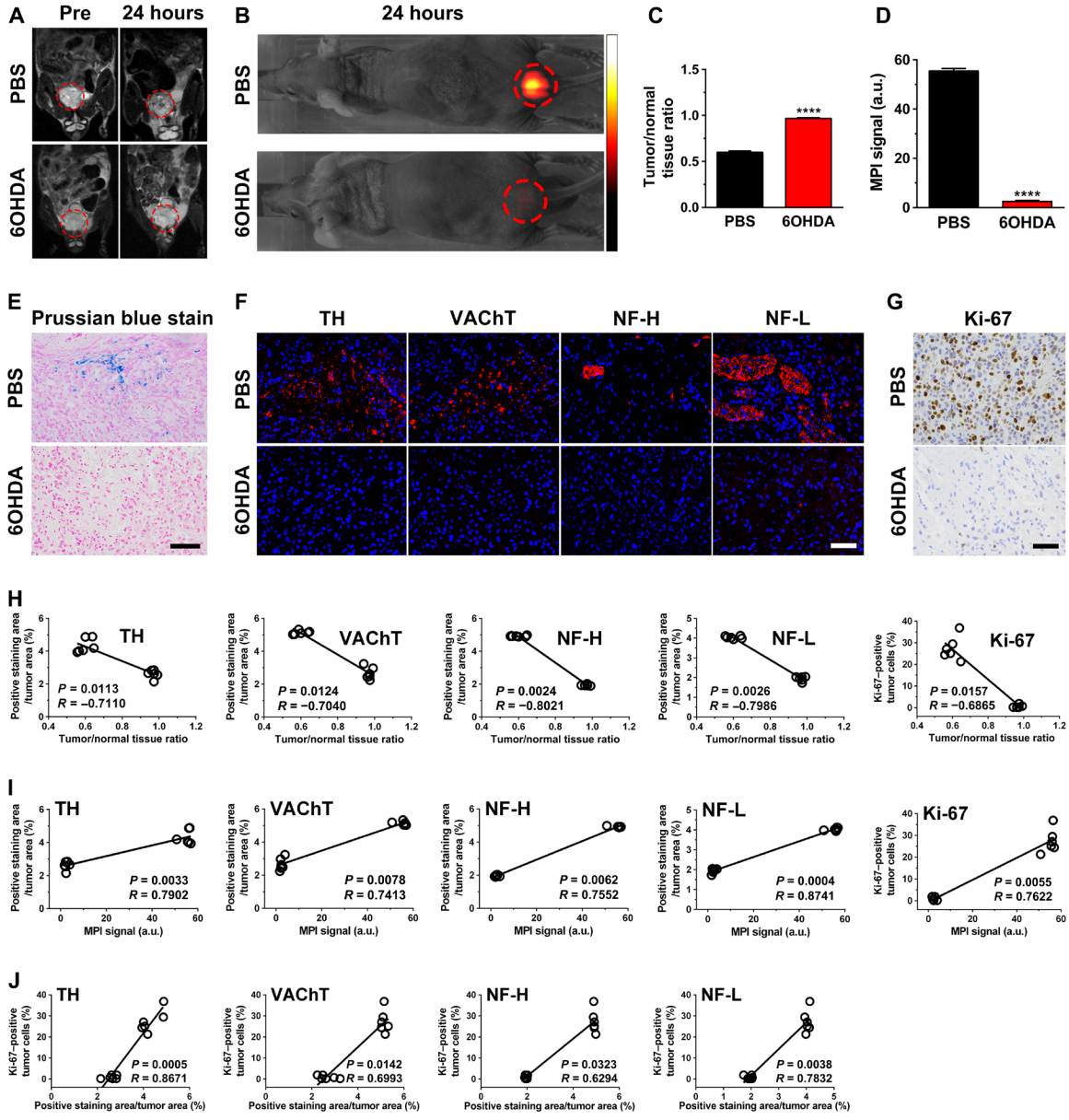

Fig. 4. PSN NPs distinguish the distribution of high and low nerve density of PCa induced by drugs. (**A** and **B**) MRI images (A) and MPI images (B) of PBS- and 6OHDA-treated mice at 24 hours after systemic administration of PSN NPs. The red dashed circles indicate the nerve density of PCa in situ. (**C** and **D**) Quantification of TNR (C) and MPI signals (D) at corresponding time points to (A) and (B), respectively. (**E**) Nuclear fast red and Prussian blue double staining images of tumor to compare the accumulation of PSN NPs in PBS- and 6OHDA-treated mice. (**F**) Immunofluorescence images of TH, VAChT, NF-H, and NF-L in PBS- and 6OHDA-treated mice. DAPI, blue; TH, VACHT, NF-H, and NF-L, red. (**G**) Immunohistochemistry images of Ki-67 in PBS- and 6OHDA-treated mice. (**H**) Pearson correlation analysis between TNR and TH, VAChT, NF-H, NF-L, and Ki-67 index, respectively. (**I**) Pearson correlation analysis between MPI signal and TH, VAChT, NF-H, NF-L, and Ki-67 index, respectively. (**J**) Pearson correlation analysis between nerve density and Ki-67 index. Spearman's correlation coefficients and *P* values are shown. Student's *t* test. Scale bars, 50 μm. Error bars represent SEM.

The results obtained in surgically treated mice were consistent with those in drug-treated mice with respect to FLI and BLI fluorescence intensities in the high- and low-nerve-density orthotopic PCa. The fluorescence intensity of surgically severed HGNx mice corresponded between immunofluorescence and immunohistochemistry (fig. S7, A to D). Moreover, four significant positive correlations were observed among fluorescence intensity and nerve density (fig. S7, E to H) and Ki-67 index (fig. S7I). These results suggest that the surgical method for the high- and low-nerve-density orthotopic PCa model is more scientific to verify the precise of nerve detection.

Together, the MRI and MPI signal intensities of the PBS-treated group and the sham-operated group were significantly associated with high nerve density of PCa upon PSN NPs systemic administration (Figs. 4, A to D, and 5, A to D). The results of MRI and MPI upon PSN NPs administration are consistent with those of FLI upon Cy7-NP41 administration in mice with PCa with high and low nerve density (figs. S5 and S7).

Downloaded from https://www.science.org on September 09, 2022

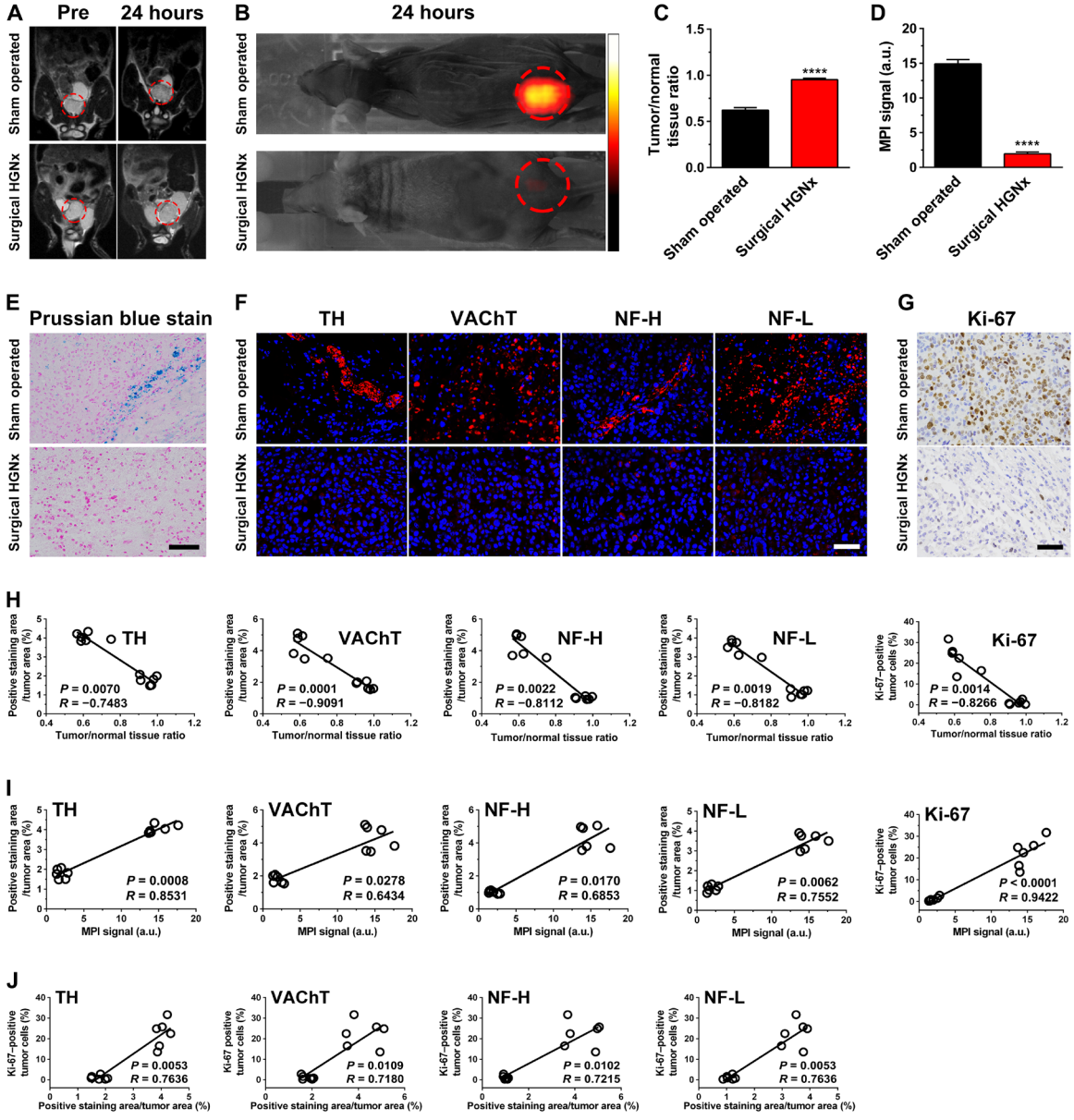

Fig. 5. PSN NPs distinguish the distribution of the high and low nerve density of PCa induced by surgery. (**A** and **B**) MRI images (A) and MPI images (B) in sham-operated and surgical HGNx–treated mice at 24 hours after systemic administration of PSN NPs. The red dashed circles indicate the nerve density of PCa in situ. (**C** and **D**) Quantification of TNR value (C) and MPI signal (D) at corresponding time points to (A) and (B), respectively. (**E**) Nuclear fast red and Prussian blue double staining images of tumor to compare the accumulation of PSN NPs in sham-operated and surgical HGNx–treated mice. (**F**) Immunofluorescence images of TH, VAChT, NF-H, and NF-L in sham-operated and surgical HGNx–treated mice. DAPI, blue; TH, VACHT, NF-H, and NF-L, red. (**G**) Immunohistochemistry images of Ki-67 in sham-operated and surgical HGNx–treated mice. (**H**) Pearson correlation analysis between TNR and TH, VAChT, NF-H, NF-L, and Ki-67 index, respectively. (**I**) Pearson correlation analysis between MPI signal and TH, VAChT, NF-H, NF-L, and Ki-67 index, respectively. (**J**) Pearson correlation analysis between nerve density and Ki-67 index. Spearman's correlation coefficients and *P* values are shown. Student's *t* test. Scale bars, 50 μm. Error bars represent SEM.

PSN NPs inhibited PCa progression through a nerve blocker

PSN NPs accumulated and localized exclusively at the tumor site. Hence, PCa progression can be inhibited by blocking the interaction of sympathetic nerves in the neural microenvironment with the tumor. We generated mouse models of orthotopic PCa using BALb/c nude male mice to mimic the natural tumor microenvironment and evaluated the effect of different treatments on orthotopic PCa progression. We monitored orthotopic PCa progression in vivo via BLI (Fig. 6A). Tumors developed rapidly in mice treated with PBS, SPIO nerve peptide NPs (SN NPs), and free propranolol (Fig. 6, A and E). PSN NPs achieved the most significant reduction in tumor growth because PSN NPs mediated the targeted delivery of propranolol to the tumor neural microenvironment. We compared the survival rates of mice treated with PBS, SN NPs, free propranolol, and PSN NPs to investigate whether PSN NPs improved the survival of mice with PCa. Consequently, the survival rate of the PSN NPs–treated mice was remarkably higher than that of mice treated with PBS, SN NPs, and free propranolol, being similar among the PBS,

Downloaded from https://www.science.org on September 09, 2022

SN NPs, and free propranolol groups (Fig. 6F). PSN NPs treatment increased the survival rate of mice to 83.3% on day 45. However, the survival rate of mice was only 46.9, 42.9, and 11.1% in the free propranolol, SN NPs, and PBS groups, respectively (Fig. 6F). These results indicate that active targeting of tumor innervation and interfering with nerve-tumor interactions potentially contribute to the improved survival rate of mice with PCa. The body weight of mice decreased gradually in the PBS, SN NPs, and free propranolol groups owing to PCa progression (Fig. 6G) but was not significantly altered after PSN NPs treatment throughout the study period (Fig. 6G). Given that PSN NPs accumulate in the liver, spleen, lungs, kidneys, and the tumor primarily, we further evaluated acute, subchronic, and chronic systemic toxicity of different formulations in healthy male BALb/c mice (6 weeks old). Quantification of typical cardiac, hepatic, and renal function indicators showed no abnormally increased levels for the PSN NPs–treated mice in comparison to those of other groups (fig. S8, A to C). In additional, hematoxylin and eosin (H&E) staining of major organs revealed no notable difference in the pathological changes between the different groups (fig. S8, D to F). Moreover, we confirmed that the delivered nerve blocker not only would not affect the normal peripheral nerve function in normal prostate tissue (fig. S9, A to D) and heart (fig. S9, E to G) but also had no side effect toward the nerve markers expression (TH, VAChT, NF-H, and NF-L) in representative normal tissues including the brain, heart, lung, stomach, intestine, liver, pancreas, spleen, adrenal gland, kidney, normal prostate tissue, and bladder (fig. S10). Consequently, these results suggest the advantages of PSN NPs for effective and safe propranolol delivery to tumors in orthotopic PCa. On day 45, the sizes of prostate tumors treated with PSN NPs were the smallest among all groups, along with the absence of lymph node metastasis (Fig. 6, B and C). Evaluation of ex vivo specimens further indicated that PSN NPs suppressed tumor progression better than PBS, SN NPs, and free propranolol.

Histological analysis of PCa tissues revealed marked retention of tumor structure upon PSN NPs treatment than upon PBS, SN NPs, and free propranolol treatment (Fig. 6C). Apoptotic cells increased markedly upon PSN NPs treatment compared with those upon treatment with PBS, SN NPs, and free propranolol (Fig. 6, D and H), suggesting that PSN NPs induce apoptosis in orthotopic prostate tumors. We evaluated the nerve density of TH, VAChT, NF-H, and NF-L in orthotopic prostate tumors; consequently, PCa tissues were infiltrated and marked with different cancer-related nerve fibers (Fig. 6I). Nerve densities were less than twofold upon treatment with PSN NPs rather than PBS, SN NPs, and free propranolol (Fig. 6, I and K). PCa progression was rapid upon treatment with PBS, SN NPs, and free propranolol, accompanied by a significant increase in intratumoral nerve density. In contrast, PSN NPs treatment inhibited tumor progression, accompanied by a reduction in nerve density of PCa tissues. Owing to symbiotic interactions between PCa and nerves (*7*), tumor growth is limited, along with a reduction in nerve density. Immunofluorescence staining of neural laminin density displayed similar trends with nerve density (Fig. 6, M and N).

The extent of PCa aggressiveness was consistent with the total extent of neurogenesis in tumor specimens (Fig. 6J). Moreover, the Ki-67 index was less than twofold upon treatment with PSN NPs in comparison with treatment with PBS, SN NPs, and free propranolol (Fig. 6L). Thus, cancer cell proliferation was significantly reduced upon treatment with PSN NPs treatment compared with that upon treatment with PBS, SN NPs, and free propranolol. Together, these results indicate that PSN NPs can block nerve function and inhibit PCa progression.

DISCUSSION

In the present study, we successfully visualized the nerve density and inhibited PCa progression through PSN NPs administration in vivo (Fig. 7). Previous studies reported that PCa is innervated, and PCa progression is linked to autonomic nerves (*1*, *2*). The application of NP41 is further supported by the innervation patterns of PCa (schematic S1). The molecular biotechnology verified the expression of the NP41 target was high in prostate tumor tissues (Fig. 1B and fig. S1). Targeting of NP41 was verified in vivo and in vitro via Cy7-NP41 (fig. S3 and Fig. 1, C to K). Various approaches have revealed that NP41 is a remarkable nerve peptide and can enhance the specificity of visualization of nerve density of PCa.

Different models of nerve density used herein for different imaging modalities to verify PSN NPs can enable visualization of nerve density of PCa with high sensitivity and specificity (Figs. 4 and 5, and figs. S5 and S7). MRI and MPI signal intensities were significantly altered upon PSN NPs treatment rather than PS NPs treatment (Fig. 3), indicating that PSN NPs facilitate highly specific visualization of nerve density of PCa on MRI and MPI. These findings are consistent with those of FLI for Cy7-NP41 and Cy7 (fig. S3). Through drug-based and surgical interventions to assess the distribution of nerve density of PCa and through imaging of the nerve density of PCa, we confirmed that PSN NPs can distinguish the high and low nerve density of PCa upon MRI and MPI (Figs. 4, A to D, and 5, A to D). Furthermore, MRI and MPI signal intensities were correlated with nerve densities and proliferation indexes (Figs. 4, H and I, and 6, H and I). Nerve densities and proliferation indexes were positively correlated with fluorescence intensity (figs. S5, E, G, H, and I, and S7, E to I), except for values of fluorescence intensity upon VAChT staining in the drug-treated groups (fig. S5F). PSN NPs helped distinguish the high and low nerve density of PCa in the surgically treated group because surgical denervation can more realistically simulate the neural microenvironment of PCa than the administration of a neurotoxic drug; moreover, PSN NPs used for MRI and MPI to visualize PCa nerve density were superior to Cy-NP41 used for FLI. A minor signal distribution was visible at the low nerve density of PCa on MPI (Figs. 4B and 5B) owing to the particles themselves being detected via MPI, rather than MRI, relative to the response they induce in surrounding tissues (*44*, *45*). These promising results strongly suggest that MPI is an ideal imaging method to visualize the nerve density of PCa. These results indicate that PSN NPs administration, combined with the advantages of MRI and MPI, facilitated not only visualization of the nerve density of PCa with high sensitivity and high specificity but also assessment of the nerve density and aggressiveness of PCa in vivo. Visualization of nerve density is a novel avenue for biomarkers for neural tissue and tumor aggressiveness in PCa and may provide strong evidence for nerve blocker treatment of PCa.

Nerve block treatment was administered at the initial stage of PCa to inhibit tumor growth (Fig. 6, A to H). The nerve density, proliferation index, and neural laminins in tumors decreased significantly upon treatment with PSN NPs, resulting in the inhibition of PCa progression (Fig. 6, I to N). PSN NPs treatment not only has no toxicity effect on other normal tissues while inhibiting the tumor

Downloaded from https://www.science.org on September 09, 2022

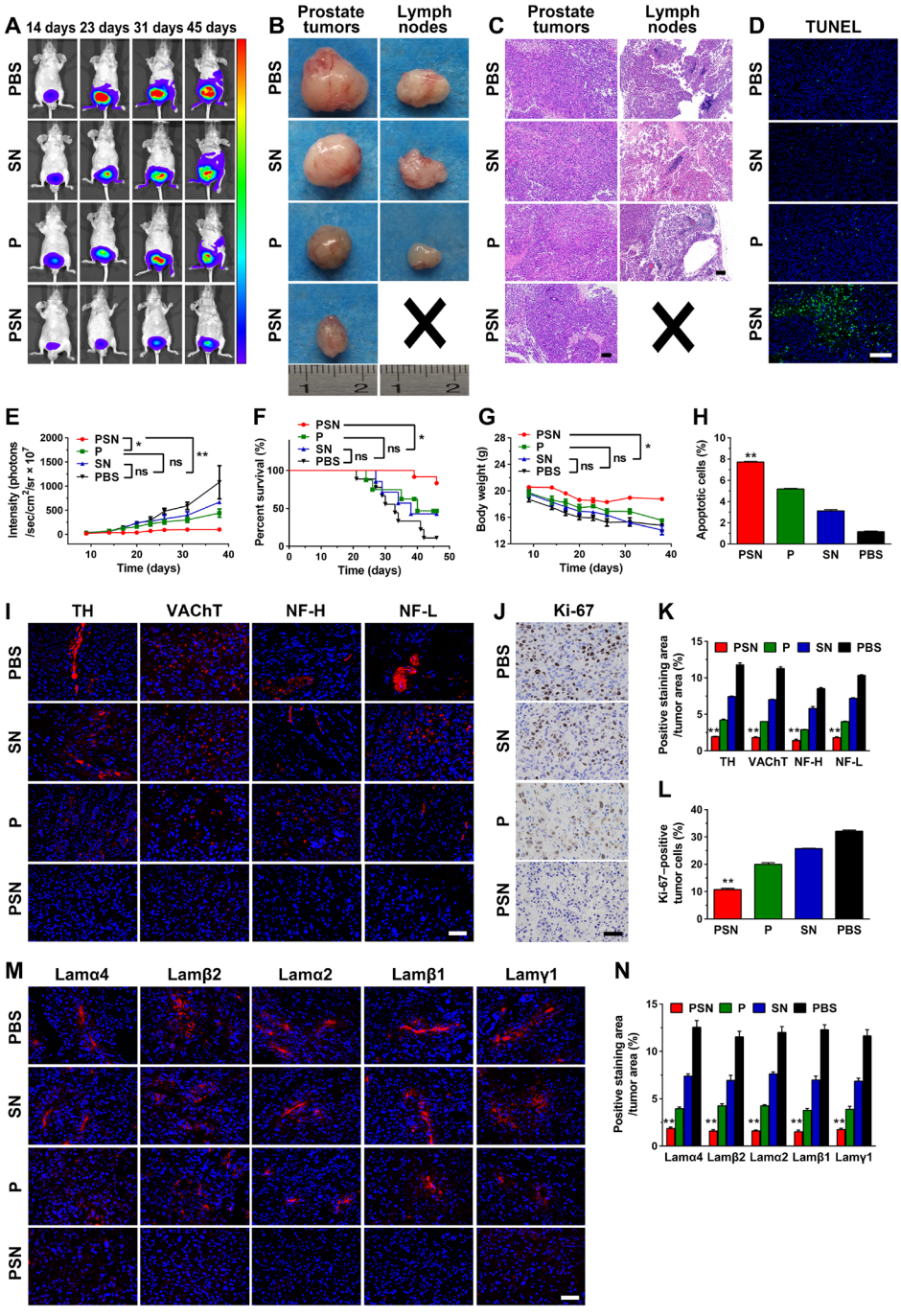

Fig. 6. PSN NPs inhibit orthotopic PCa development. PC-3luc cells were injected into the ventral prostate of BALb/c nude male mice to form orthotopic PCa on day 0. After 10 days, mice were divided into different groups: PBS, SN NPs, free propranolol (P), and PSN NPs. Mice received various formulations by systemic administration for six times. (**A**) In vivo bioluminescence images indicate the orthotopic PCa development on days 14, 23, 31, and 45 after orthotopic PC-3luc cell xenografts. (**B**) Images of orthotopic prostate tumors (left) and lymph nodes (right) on day 45. (**C**) H&E staining sections of orthotopic prostate tumors (left) and lymph nodes (right) from indicated groups. (**D**) TUNEL (terminal deoxynucleotidyl transferase–mediated deoxyuridine triphosphate nick end labeling) of apoptotic cells in tumors from indicated groups. (**E**) Serial quantification of in vivo bioluminescence intensity of xenografts in the prostate gland. ns, not significant. (**F**) The mice survival curves in different groups, evaluated by the Kaplan-Meier method and the log-rank test. (**G**) The changes of mice body weight during treatments. (**H**) Quantification of apoptotic TUNEL$^+$ cells in the orthotopic prostate tumors from indicated groups at posttreatment. (**I**) Immunofluorescence images of TH, VAChT, NF-H, and NF-L from indicated groups after treatment. DAPI, blue; TH, VACHT, NF-H, and NF-L, red. (**J**) Immunohistochemistry images of Ki-67 from indicated groups after treatment. (**K**) Quantification of nerve density of TH, VAChT, NF-H, and NF-L. (**L**) Quantification of Ki-67 index. (**M**) Immunofluorescence images of lamα4, lamβ2, lamα2, lamβ1, and lamγ1 after treatments. DAPI, blue; lamα4, lamβ2, lamα2, lamβ1, and lamγ1, red. (**N**) Quantification of laminin density of lamα4, lamβ2, lamα2, lamβ1, and lamγ1. Data were obtained from five fields per section from field surface of 0.27 mm^2. *P < 0.05, **P < 0.01, and ns, P > 0.05. The statistical analysis was based on nonparametric one-way analysis with Kruskal-Wallis. Scale bars, 50 μm. Error bars represent SEM (n = 7 to 12 per group).

Downloaded from https://www.science.org on September 09, 2022

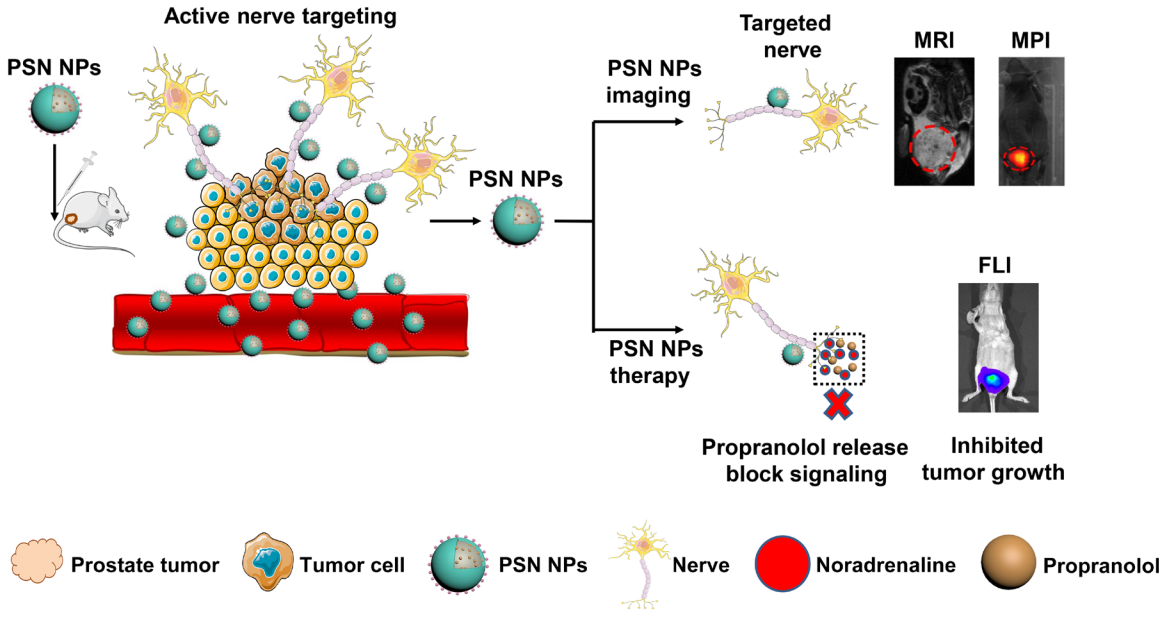

Fig. 7. Illustration of nerve density visualization by MRI and MPI with high sensitivity and specificity and targeted delivery of the nerve blocker propranolol to effectively inhibit PCa progression.

progression (Fig. 6G and fig. S8) but also has no side effect toward the nerve function (fig. S9) and the nerve marker expression (fig. S10) in those normal tissues. These results elucidate the performance of drug-loaded synthetic nanoprobes for targeted delivery of the neural drug propranolol to interfere with the effects of nerves on PCa.

In summary, we successfully visualized the nerve density of tumors using PSN NPs and via MRI and MPI, which enabled the assessment of nerve densities of PCa in vivo, providing information regarding PCa invasiveness. Various xenogeneic PCa models with high and low nerve density were generated to verify the effectiveness of PSN NPs in visualizing nerve density. Furthermore, PSN NPs inhibited PCa progression by blocking nerve function. Our study describes the successful development of an approach to visualize nerve density of PCa, with high sensitivity and specificity and for targeting delivery of the nerve blocker propranolol to effectively inhibit PCa progression.

MATERIALS AND METHODS

Preparation and characterization of Cy7-NP41

Nerve-binding peptide (NP41, China Peptides Co. Ltd.) was labeled with Cy7 monosuccinimidyl ester (Cy7-NHS; AAT Bioquest Inc.) at 25°C as in a previous study (*46*). Briefly, Cy7-NHS and NP41 were dissolved in dimethyl sulfoxide (Aladdin), respectively. After overnight shaking in darkness, the product was dialyzed for 24 hours to remove unconjugated Cy7-NHS or NP41. Last, the product was lyophilized to obtain Cy7-NP41. The fluorescence intensity of Cy7-NP41 was measured at various concentrations (0, 0.3, 0.6, 1.25, 2.5, 5, 10, 20, 40, 80, and 159 μM). The steady conjugation of Cy7-NHS and NP41 was characterized by mass spectroscopy. Both optical absorption spectra of the Cy7-NP41 and Cy7-NHS were acquired by a UV-vis spectrophotometer (UV3600, Shimadzu, Japan). Fluorescence excitation and emission spectrum were monitored using a fluorescence spectrofluorometer (F-7000, Hitachi, Japan). The optical absorption peaks of Cy7-NP41 and Cy7 dissolved in fetal bovine serum (FBS; Gibco) were monitored at different time points over 48 hours. All reactions were performed in the dark. The cytotoxicity of the Cy7-NP41 was evaluated by Cell Counting Kit-8 (CCK-8 assay, Solarbio).

Synthesis of SPIO@OA NPs

For synthesis of the oleic acid (OA; Aladdin)–coated iron oxide NPs (SPIO@OA NPs), we adopted a thermal decomposition method based on a previous publication (*40*). In detail, 2.3 ml of OA, 1.7 ml of oleylamine (OAm; Aladdin), and 20 mL of dibenzyl ether (Aladdin) were added to 0.7 g of ferric acetylacetonate (Aladdin) placed in a 50-ml three-neck flask. The mixture was stirred under the protection of nitrogen (N_2) and then heated to 220°C (nucleation temperature) at a heating rate of 3.3°C/min (60 min) by a program temperature control device and maintained for 1 hour. Subsequently, the temperature of the reaction was heated to 300°C (maturation temperature) and kept for 10 hours. Last, the product was ultrasonically dissolved and magnetically separated by a strong magnet three times to remove residual OA, OAm, and dibenzyl ether and then was decentralize in 10 ml of chloroform (Aladdin).

Synthesis of PS NPs

In a typical synthesis, 50 mg of DSPE-mPEG2000 (N-(Carbonyl-methoxypolyethylene glycol 2000)-1,2-distearoyl-sn-glycerol-3-phosphoethanolamine,sodium salt) (A.V.T. Pharmaceutical Co. Ltd.), 50 mg of DSPE-PEG2000-COOH (1,2-distearoyl-sn-glycero-3-phosphoethanolamine-N-[(polyethylene glycol)-2000]-carboxylic acid) (A.V.T. Pharmaceutical Co. Ltd.), and 10 mg of propranolol (Sigma-Aldrich) were added to a 10-ml round-bottom flask and dissolved in 4 ml of chloroform, and 10 mg of SPIO@OA NPs was added, followed by 2 ml of deionized water and ultrasonically mixed in the system. Subsequently, the mixture was rotary evaporated at 70°C until the chloroform was completely volatilized. Last, the monodispersed PS NPs were achieved.

Downloaded from https://www.science.org on September 09, 2022

Synthesis of PSN NPs

The PSN NPs were synthesized by the following procedures. At first, 10 mg of PS NPs were resuspended in 10 ml of 2-morpholinoethanesulfonic (MES) acid (Sigma-Aldrich) buffer (0.02 M, pH, 5.5), and 10 μmol of *N*-(3-dimethylaminopropyl)-*N*′-ethylcarbodiimide hydrochloride (EDC; Sigma-Aldrich) and 10 μmol of NHS (Sigma-Aldrich) were added in it to activate the carboxyl groups. The reactants were stirred for 30 min at 25°C. Then, free EDC and NHS were removed using the ultrafiltration centrifuge tube (100 kDa, molecular weight cutoff, 3000*g*, 10 min) with deionized water for three times. Then, the above products were resuspended using the NP41 (0.2 mM) previously dissolved in PBS buffer and stirred continuously at 25°C for 2 hours. Free NP41 was removed by ultrafiltration centrifuge tube with deionized water for three times. Last, the resulting ultrafiltrate was used to measure the labeling efficiency by a UV-vis spectrophotometer. The product was lastly filtered, exploiting a 220-nm filtering membrane and stored at 4°C. The synthetic route was according to Fig. 2A.

Characterization of PSN NPs

The size and morphology of PS NPs and PSN NPs were observed by TEM (JEOL-1011, Tokyo, Japan). The peptide on PSN NPs was evaluated using a UV-vis spectrophotometer, applying the following formula: labeling efficiency of peptide (%) = [peptide input (mg) − peptide in supernatant (mg)]/peptide input (mg) × 100%. Before this, we first calculated the relationship between concentration and absorption peak of free peptide by a UV-vis spectrophotometer (table S1). The hydrated particle size distribution and zeta potential were characterized using a Malvern Zetasizer (ZEN 3600, UK). The T2WI was carried out on a clinical 3.0-T MRI scanner (Skyra, Siemens, Germany). PSN NPs stock solution of 0.279 mM was serially diluted and placed in a 96-well plate to detect the MRI signal. The MPI signal was acquired on an MPI (MOMENTUM, MagneticInsight, USA). PSN NPs stock solution of 17.857 mM was serially diluted, and 1-μl point sources with concentration of 16.071, 14.286, 12.500, 10.714, 8.929, and 7.142 mM were prepared to detect the MPI signal. Magnetism was observed by a vibrating sample magnetometer (Yingpu Magnetic Technology Development Co. Ltd., China).

Propranolol release from PSN NPs

In vitro propranolol release from PSN NPs was determined by HPLC using a Shim-pack VP-ODS C18 column (250 mm by 4.6 mm, 5 μm, Shimadzu) with mobile phase of 0.05 mol/liter potassium dihydrogen phosphate containing 0.1% sodium heptane sulfonate-methanol (43:57). The flow rate was 1.0 ml/min, and the detection wavelength was 290 nm. In vitro propranolol released profiles from PSN NPs in buffer at pH 6.0 and 7.4, which simulate the PH conditions of tumor microenvironment and normal physiological condition, respectively.

Cell culture

The human PCa cell line PC-3 cells stably transfected with luciferase genes (PerkinElmer) were cultured according to the manufacturer's recommendations in minimum essential medium supplemented with 10% FBS and 1% penicillin/streptomycin. The PC-3luc cells were routinely maintained in a humidified atmosphere containing 5% CO_2 incubator at 37°C. In addition to Dulbecco's modified Eagle's medium, the culture method of DU-145luc cells (American Type Culture Collection) was the same as that of PC-3luc cells.

Experimental animals

The protocols were approved by the ethics committee of Tongji Hospital, Tongji Medical College, Huazhong University of Science and Technology. The orthotopic PCa was created to mimic the natural PCa microenvironment. Briefly, BALb/c nude mice (male, 6 to 8 weeks of age) were purchased from Beijing Vital River Laboratory Animal Technology Co. Ltd. (China) and raised under specific-pathogen–free conditions. Mice were anesthetized, a midline incision was made in the pelvic of the mice, and approximately 1×10^6 PC-3luc PCa cells in Matrigel were injected into the ventral prostate of the mice using insulin syringes. The incision was closed by 7-0 silk. For chemical sympathectomy, 10 days after PC-3luc cell injection (day 0), the animals were randomly divided into the different groups and received PBS or 6OHDA (Sigma-Aldrich) at day 0 (100 mg/kg) and day 2 (250 mg/kg) by intraperitoneal injection. For the surgical denervation, the afferent hypogastric nerves of the animals were surgically cut before orthotopic implantations of PC-3 cells.

Bioluminescence imaging

The orthotopic PCa progression was monitored by BLI using an IVIS Spectrum imaging system (IVIS Spectrum, PerkinElmer, USA). The bioluminescent signal was produced via the interaction of luciferase from PC-3luc cells with the D-luciferin solution (100 μl; 15 mg/ml; PerkinElmer) intraperitoneally injected into the mice before the in vivo imaging. Mice were anesthetized using 2% isoflurane/air gas mixture during the whole imaging process. Ten days after implantation, the tumor-bearing mice were observed by IVIS Spectrum and randomized to diverse imaging and treatments.

Near-infrared FLI

After 11 weeks of orthotopic PCa development, a time enough for tumors to interact with the nervous microenvironment, the tumor-bearing mice were intravenously injected with Cy7-NP41 (100 μg/ml; 100 μl, experimental group) and Cy7 (100 μg/ml; 100 μl, control group), respectively. To observe the biodistribution of Cy7-NP41 and Cy7 in vivo, FLI was conducted at different time points after injection (30 min, 2 hours, 4 hours, 6 hours, 12 hours, 24 hours, and 48 hours) by IVIS Spectrum. Cy7-NP41 aggregated in the tumor region after 8 hours and then the orthotopic prostate tumor was exposed by a skin midline incision over the pelvic. The PBS group, 6OHDA group, sham-operated group, and HGNx group, respectively, were treated with intravenous Cy7-NP41 (at the corresponding concentration and volume). At 48 hours after injection, mice were euthanized, and tumor tissues and major organs including the heart, liver, spleen, lung, and kidney were dissected carefully for ex vivo FLI and observed with the same imaging system. The region of interest (ROI) of the tumor and muscle regions was drawn to calculate the TNR, and the fluorescence intensity of the tumors and the major organs was quantitatively analyzed by IVIS Living Imaging 4.4 software.

3D imaging of FLI and BLI

We used the Photon Imager (Biospace Lab S.A., France), having the advantages of high-throughput, high-resolution, and multispectral analysis, to colocalize the bioluminescent signal and fluorescence signal of the orthotopic PCa. First, the laser scanned the surface topology (including the surface contour and the overall shape of the structure). Then, the 3D module cooperated with the intensified charge-coupled device for optical signal reception. The Atlas coregistration

Downloaded from https://www.science.org on September 09, 2022

tool combined 3D module acquisition data with anatomical information from the Digimouse Atlas (University of Southern California) to locate the organ of the optical signal. Volumetric bioluminescent signal and fluorescence signal from the 3D module data were reconstructed using the M3Vision Analysis Software (Biospace Lab).

Magnetic resonance imaging

In vivo orthotopic PCa MRI was performed by a 1.5-T MRI scanner (M3TM, Aspect Imaging, Israel) using a 38-mm circular coil and a mouse cradle. Mice were anesthetized using 2% isoflurane/air gas mixture. The parameters of T2WI were as follows: repetition time, 6000 ms; echo time, 66.61 ms; flip angle, 90°; slice orientation: coronal; field of view, 30 mm by 60 mm; matrix size, 256 × 128; number of slices, 20; and slice thickness, 1 mm. To compare the changes of signal intensity in the tumor site, MRI was conducted before and after systemic administration of PSN NPs (6 mg/kg, experimental group) and PS NPs (6 mg/kg, control group) at appropriate time points. PSN NPs (at the corresponding concentration and volume) were treated intravenously in the PBS group, 6OHDA group, sham-operated group, and HGNx group, respectively. ROI of the tumor and muscle regions was drawn to calculate the TNR by RadiAntviewer (Medixant, Poland).

Magnetic particle imaging

Mice with orthotopic PCa were injected with PSN NPs (at the corresponding concentration and volume) through the tail vein. MPI was performed on each mouse 24 hours after injection. Representative maximum intensity projection images of the MPI data were overlaid on corresponding photographs using fiducial markers to coregister the two modalities. Data analysis was performed with the VivoQuant software (Invicro LLC, USA). ROIs were drawn around the tumor to quantify MPI signal.

Orthotopic PCa progression

PC-3luc cells were injected into the ventral prostate of BALb/c nude male mice to form orthotopic PCa on day 0. Ten days after the PC-3luc cell implantation, the mice were randomly divided into different groups (n = 7 to 12 per group) and treated with PBS, SN NPs (6 mg/kg), free propranolol (5 mg/kg), and PSN NPs (6 mg/kg) through intravenous injection in the tail in 100-μl volume for each formulation on a predefined time point. The treatment was carried out twice a week for 3 weeks. Tumor progression was monitored by BLI. Mice body weights were measured during the experiment. Mice were monitored for up to 45 days after implantation and then euthanized.

In vivo safety evaluation

Serum biochemical analysis and H&E staining were used to evaluate the systemic toxicity of PSN NPs. Different formulations, including PBS, SN NPs, free propranolol, and PSN NPs, were injected to healthy male BALb/c mice (6 weeks old). Blood samples were extracted from PBS, SN NPs, free propranolol, and PSN NPs mice groups at acute, subchronic, and chronic times. To separate serum, fresh blood samples were collected via the ocular vein (0.8 to 1.5 ml for each mouse) and then centrifuged twice (3500 rpm, 10 min). The important indicators of cardiac, hepatic, and renal function including alanine aminotransferase, aspartate aminotransferase, total protein, albumin, globulin, creatine kinase, L-lactate dehydrogenase, urea, creatinine, and uric acid were measured using an automatic biochemical analyzer (cobas 8000, Roche, Germany). Major organs including the brain, heart, lung, liver, spleen, and kidney were isolated at acute, subchronic, and chronic times for H&E staining.

Assessment of cardiac function

Cardiac function was assessed by echocardiography using the Mindray Resona7 ultrasound imaging system, in which mice were treated for PSN NPs and PBS according to the protocol described above (n = 5 per group). For imaging, animals were anesthetized with 2% isoflurane/air gas mixture and then positioned ventral side up on the platform of the imaging system. Cardiac examinations were performed in 2D images using the parasternal long axis view in B-mode with a 20-MHz probe. Systolic and diastolic images of the left ventricle were acquired by M-mode. The left ventricular end-diastolic volume and left ventricular end-systolic volume were determined to calculate the ejection fraction.

Assessment of prostatic innervation

The weight measurement, DNA determination, and prostate binding protein (PBP) expression of the ventral prostate after treatment of PSN NPs and PBS were measured as performed in a previous study (*47*, *48*).

Histologic staining

Researchers were blinded to group assignation of mice tissues for histopathologic examinations. Paraffin sections (thickness, 4 μm) were stained with H&E and double stained with nuclear fast red and Prussian blue. Immunofluorescence and immunohistochemistry were performed as previously described (*1*).We used immunofluorescence and immunohistochemistry to evaluate the nerve densities and cell proliferation. Antibodies and staining reagents used were as follows: anti-TH (AB152) and anti–NF-L (AB9568) were purchased from Millipore (Germany); anti-VAChT (H-V007) was from Phoenix Pharmaceuticals (Burlingame CA, USA); anti–NF-H (ab8135), anti–laminin-α2 (ab11576), anti–laminin-β1 (ab44941), and anti–laminin-γ1 (ab80580) were from Abcam (Cambridge, MA, USA); anti–laminin-β2 (sc-135967) was from Santa Cruz Biotechnology (USA); and anti–laminin-α4 (ABP51699) was from Abbkine (USA). TUNEL (terminal deoxynucleotidyl transferase–mediated deoxyuridine triphosphate nick end labeling) kit staining was performed using a kit (Roche, Switzerland) according to the manufacturer's instructions. Anti–β-actin (26616) was from Thermo Fisher Scientific (USA). Perls stain (PN0110), nuclear fast red (PN0115), and H&E stain (PN0004) were from Pinuofeibiotechnology (China). Anti–Ki-67 (ARG53222) was from Arigobio (China). DAPI (4′,6-diamidino-2-phenylindole) (C0060), bovine serum albumin (A8020), and CCK-8 assay were from Solarbio (USA). To quantify the nerve density and laminin density, five independent fields (0.27 mm^2) within the sections were randomly selected. The Image-Pro Plus software (Media Cybernetics, Rockville, MD, USA) was used to provide density measurements for the images, and the overall nerve density and laminin density were evaluated by counting the nerve and laminin areas per field by setting the same threshold. To quantify the Ki-67 index, the same blue nuclei were selected as total cells, and the percentage of positive cells (positive cells/total cells × 100%) was the positive rate.

Western blot

The expression of laminins in orthotopic PCa was assessed by Western blot assay. The band intensity of proteins was quantified

Downloaded from https://www.science.org on September 09, 2022

by the AlphaEaseFC software. Antibodies used were as follows: anti–laminin-β1 (sc-33709), anti–laminin-β2 (sc-135967), and anti–laminin-α2 (sc-59854, clone 4H8-2) were from Santa Cruz Biotechnology (USA); anti–laminin-γ1 (ab233389) and anti-PBP (ab76582) were from Abcam (Cambridge, MA, USA); and anti–laminin-α4 (ABP51699) was from Abbkine (USA).

Statistical analysis

All data analysis in this study was carried out using GraphPad Prism 6 or SPSS Statistics 24. The samples and animals were allocated to experimental groups and processed randomly. All in vitro experiments represented multiple independent experiments conducted in triplicate. The in vivo experiments were performed with 3 to 12 mice for each condition. All data are represented as means ± SEM. Statistically different significance between groups was determined by unpaired two-tailed Student's *t* tests or nonparametric one-way analysis with Kruskal-Wallis. Regression models were used to estimate the magnitude of the association. Correlations between variables were evaluated using the Spearman rank correlation test. The Kaplan-Meier method was used to illustrate the survival curves, and the log-rank test was used to determine the statistical significance of the difference between survival curves. $P < 0.05$ was considered statistically significant.

SUPPLEMENTARY MATERIALS

Supplementary material for this article is available at http://advances.sciencemag.org/cgi/content/full/6/6/eaax6040/DC1

Schematic S1. PCa innervation.
Fig. S1. Expression of neural laminins in prostate tumor tissues and healthy prostate tissues.
Fig. S2. Characterization of Cy7-NP41.
Fig. S3. The targeting of NP41 in vivo.
Fig. S4. Orthotopic PCa with high and low nerve density constructed by PBS and 6OHDA.
Fig. S5. FLI of high and low nerve density of PCa in PBS- or 6OHDA-treated mice.
Fig. S6. Orthotopic PCa with high and low nerve density constructed by sham-operated nerve-intact and surgically severed afferent hypogastric nerves.
Fig. S7. FLI of high and low nerve density of PCa in sham-operated or surgical HGNx mice.
Fig. S8. Acute, subchronic, and chronic toxicity evaluation of PSN NPs after intravenous injection in health mice.
Fig. S9. Evaluation of health mice nerve function after PSN NPs systemic administration for six times.
Fig. S10. Evaluation of health mice nerve marker expression after PSN NPs systemic administration for six times.
Table S1. Correlation between concentration of peptides and optical absorption peak at 280 nm.

REFERENCES AND NOTES

1. C. Magnon, S. J. Hall, J. Lin, X. Xue, L. Gerber, S. J. Freedland, P. S. Frenette, Autonomic nerve development contributes to prostate cancer progression. *Science* **341**, 1236361 (2013).
2. A. H. Zahalka, A. Arnal-Estape, M. Maryanovich, F. Nakahara, C. D. Cruz, L. W. S. Finley, P. S. Frenette, Adrenergic nerves activate an angio-metabolic switch in prostate cancer. *Science* **358**, 321–326 (2017).
3. K. Dobrenis, L. R. Gauthier, V. Barroca, C. Magnon, Granulocyte colony-stimulating factor off-target effect on nerve outgrowth promotes prostate cancer development. *Int. J. Cancer* **136**, 982–988 (2015).
4. J. R. Keast, Visualization and immunohistochemical characterization of sympathetic and parasympathetic neurons in the male rat major pelvic ganglion. *Neuroscience* **66**, 655–662 (1995).
5. S. Hassan, Y. Karpova, D. Baiz, D. Yancey, A. Pullikuth, A. Flores, T. Register, J. M. Cline, R. D'Agostino Jr., N. Danial, S. R. Datta, G. Kulik, Behavioral stress accelerates prostate cancer development in mice. *J. Clin. Invest.* **123**, 874–886 (2013).
6. G. E. Ayala, H. Dai, M. Powell, R. Li, Y. Ding, T. M. Wheeler, D. Shine, D. Kadmon, T. Thompson, B. J. Miles, M. M. Ittmann, D. Rowley, Cancer-related axonogenesis and neurogenesis in prostate cancer. *Clin. Cancer Res.* **14**, 7593–7603 (2008).
7. G. E. Ayala, T. M. Wheeler, H. D. Shine, M. Schmelz, A. Frolov, S. Chakraborty, D. Rowley, In vitro dorsal root ganglia and human prostate cell line interaction: Redefining perineural invasion in prostate cancer. *Prostate* **49**, 213–223 (2001).
8. N. Mottet, J. Bellmunt, M. Bolla, E. Briers, M. G. Cumberbatch, M. De Santis, N. Fossati, T. Gross, A. M. Henry, S. Joniau, T. B. Lam, M. D. Mason, V. B. Matveev, P. C. Moldovan, R. C. N. van den Bergh, T. Van den Broeck, H. G. van der Poel, T. H. van der Kwast, O. Rouviere, I. G. Schoots, T. Wiegel, P. Cornford, EAU-ESTRO-SIOG guidelines on prostate cancer. Part 1: Screening, diagnosis, and local treatment with curative intent. *Eur. Urol.* **71**, 618–629 (2017).
9. P. Cornford, J. Bellmunt, M. Bolla, E. Briers, M. De Santis, T. Gross, A. M. Henry, S. Joniau, T. B. Lam, M. D. Mason, H. G. van der Poel, T. H. van der Kwast, O. Rouviere, T. Wiegel, N. Mottet, EAU-ESTRO-SIOG guidelines on prostate cancer. Part II: Treatment of relapsing, metastatic, and castration-resistant prostate cancer. *Eur. Urol.* **71**, 630–642 (2017).
10. F.-Y. Cheng, C.-H. Su, Y.-S. Yang, C.-S. Yeh, C.-Y. Tsai, C.-L. Wu, M.-T. Wu, D.-B. Shieh, Characterization of aqueous dispersions of Fe3O4 nanoparticles and their biomedical applications. *Biomaterials* **26**, 729–738 (2005).
11. R. Qiao, C. Yang, M. Gao, Superparamagnetic iron oxide nanoparticles: From preparations to in vivo MRI applications. *J. Mater. Chem.* **19**, 6274–6293 (2009).
12. N. Lee, T. Hyeon, Designed synthesis of uniformly sized iron oxide nanoparticles for efficient magnetic resonance imaging contrast agents. *Chem. Soc. Rev.* **41**, 2575–2589 (2012).
13. C. Xu, S. Sun, New forms of superparamagnetic nanoparticles for biomedical applications. *Adv. Drug Deliv. Rev.* **65**, 732–743 (2013).
14. M. R. Bashir, L. Bhatti, D. Marin, R. C. Nelson, Emerging applications for ferumoxytol as a contrast agent in MRI. *J. Magn. Reson. Imaging* **41**, 884–898 (2015).
15. J. P. Netto, J. Iliff, D. Stanimirovic, K. A. Krohn, B. Hamilton, C. Varallyay, S. Gahramanov, H. Daldrup-Link, C. d'Esterre, B. Zlokovic, H. Sair, Y. Lee, S. Taheri, R. Jain, A. Panigrahy, D. S. Reich, L. R. Drewes, M. Castillo, E. A. Neuwelt, Neurovascular unit: Basic and clinical imaging with emphasis on advantages of ferumoxytol. *Neurosurgery* **82**, 770–780 (2018).
16. B. Gleich, J. Weizenecker, Tomographic imaging using the nonlinear response of magnetic particles. *Nature* **435**, 1214–1217 (2005).
17. R. M. Ferguson, A. P. Khandhar, S. J. Kemp, H. Arami, E. U. Saritas, L. R. Croft, J. Konkle, P. W. Goodwill, A. Halkola, J. Rahmer, J. Borgert, S. M. Conolly, K. M. Krishnan, Magnetic particle imaging with tailored iron oxide nanoparticle tracers. *IEEE Trans. Med. Imaging* **34**, 1077–1084 (2015).
18. A. P. Khandhar, R. M. Ferguson, H. Arami, K. M. Krishnan, Monodisperse magnetite nanoparticle tracers for in vivo magnetic particle imaging. *Biomaterials* **34**, 3837–3845 (2013).
19. J. Weizenecker, B. Gleich, J. Rahmer, H. Dahnke, J. Borgert, Three-dimensional real-timein vivomagnetic particle imaging. *Phys. Med. Biol.* **54**, L1–L10 (2009).
20. Y. Du, P. T. Lai, C. H. Leung, P. W. Pong, Design of Superparamagnetic Nanoparticles for Magnetic Particle Imaging (MPI). *Int. J. Mol. Sci.* **14**, 18682–18710 (2013).
21. R. M. Ferguson, K. R. Minard, K. M. Krishnan, Optimization of nanoparticle core size for magnetic particle imaging. *J. Magn. Magn. Mater.* **321**, 1548–1551 (2009).
22. J. Weizenecker, J. Borgert, B. Gleich, A simulation study on the resolution and sensitivity of magnetic particle imaging. *Phys. Med. Biol.* **52**, 6363–6374 (2007).
23. T. Knopp, S. Biederer, T. F. Sattel, M. Erbe, T. M. Buzug, Prediction of the spatial resolution of magnetic particle imaging using the modulation transfer function of the imaging process. *IEEE Trans. Med. Imaging* **30**, 1284–1292 (2011).
24. P. W. Goodwill, E. U. Saritas, L. R. Croft, T. N. Kim, K. M. Krishnan, D. V. Schaffer, S. M. Conolly, X-Space MPI: Magnetic nanoparticles for safe medical imaging. *Adv. Mater.* **24**, 3870–3877 (2012).
25. E. Y. Yu, M. Bishop, B. Zheng, R. M. Ferguson, A. P. Khandhar, S. J. Kemp, K. M. Krishnan, P. W. Goodwill, S. M. Conolly, Magnetic particle imaging: A novel in vivo imaging platform for cancer detection. *Nano Lett.* **17**, 1648–1654 (2017).
26. G. Song, M. Chen, Y. Zhang, L. Cui, H. Qu, X. Zheng, M. Wintermark, Z. Liu, J. Rao, Janus iron oxides @ semiconducting polymer nanoparticle tracer for cell tracking by magnetic particle imaging. *Nano Lett.* **18**, 182–189 (2018).
27. M. A. Whitney, J. L. Crisp, L. T. Nguyen, B. Friedman, L. A. Gross, P. Steinbach, R. Y. Tsien, Q. T. Nguyen, Fluorescent peptides highlight peripheral nerves during surgery in mice. *Nat. Biotechnol.* **29**, 352–356 (2011).
28. H. L. Glasgow, M. A. Whitney, L. A. Gross, B. Friedman, S. R. Adams, J. L. Crisp, T. Hussain, A. P. Frei, K. Novy, B. Wollscheid, Q. T. Nguyen, R. Y. Tsien, Laminin targeting of a peripheral nerve-highlighting peptide enables degenerated nerve visualization. *Proc. Natl. Acad. Sci. U.S.A.* **113**, 12774–12779 (2016).
29. D. V. Hingorani, M. A. Whitney, B. Friedman, J. K. Kwon, J. L. Crisp, Q. Xiong, L. Gross, C. J. Kane, R. Y. Tsien, Q. T. Nguyen, Nerve-targeted probes for fluorescence-guided intraoperative imaging. *Theranostics* **8**, 4226–4237 (2018).
30. A. P. Wu, M. A. Whitney, J. L. Crisp, B. Friedman, R. Y. Tsien, Q. T. Nguyen, Improved facial nerve identification with novel fluorescently labeled probe. *Laryngoscope* **121**, 805–810 (2011).

Downloaded from https://www.science.org on September 09, 2022

31. T. Hussain, M. B. Mastrodimos, S. C. Raju, H. L. Glasgow, M. Whitney, B. Friedman, J. D. Moore, D. Kleinfeld, P. Steinbach, K. Messer, M. Pu, R. Y. Tsien, Q. T. Nguyen, Fluorescently labeled peptide increases identification of degenerated facial nerve branches during surgery and improves functional outcome. *PLOS ONE* **10**, e0119600 (2015).
32. Y. Jiang, N. Quyen, M. Whitney, D. Hingorani, G. Ihn, R. K. Mittal, Vagal innervation of the esophagus and stomach: Visualized using a novel nerve peptide (NP41). *Gastroenterology* **152**, S932–S932 (2017).
33. D. Palm, K. Lang, B. Niggemann, T. L. t. Drell, K. Masur, K. S. Zaenker, F. Entschladen, The norepinephrine-driven metastasis development of PC-3 human prostate cancer cells in BALB/c nude mice is inhibited by β-blockers. *Int. J. Cancer* **118**, 2744–2749 (2006).
34. H. H. Grytli, M. W. Fagerland, S. D. Fosså, K. A. Taskén, L. L. Haheim, Use of β-blockers is associated with prostate cancer-specific survival in prostate cancer patients on androgen deprivation therapy. *Prostate* **73**, 250–260 (2013).
35. H. H. Grytli, M. W. Fagerland, S. D. Fossa, K. A. Tasken, Association between use of β-blockers and prostate cancer-specific survival: A cohort study of 3561 prostate cancer patients with high-risk or metastatic disease. *Eur. Urol.* **65**, 635–641 (2014).
36. J. Mosayebi, M. Kiyasatfar, S. Laurent, Synthesis, functionalization, and design of magnetic nanoparticles for theranostic applications. *Adv. Healthc. Mater.* **6**, 1700306 (2017).
37. T. Vangijzegem, D. Stanicki, S. Laurent, Magnetic iron oxide nanoparticles for drug delivery: Applications and characteristics. *Expert Opin. Drug Deliv.* **16**, 69–78 (2019).
38. G. Hong, A. L. Antaris, H. Dai, Near-infrared fluorophores for biomedical imaging. *Nat. Biomed. Eng.* **1**, 0010 (2017).
39. J. Cao, S. Wan, J. Tian, S. Li, D. Deng, Z. Qian, Y. Gu, Fast clearing RGD-based near-infrared fluorescent probes for in vivo tumor diagnosis. *Contrast Media Mol. Imaging* **7**, 390–402 (2012).
40. L. Chen, J. Xie, H. Wu, F. Zang, M. Ma, Z. Hua, N. Gu, Y. Zhang, Improving sensitivity of magnetic resonance imaging by using a dual-targeted magnetic iron oxide nanoprobe. *Colloids Surf. B* **161**, 339–346 (2018).
41. Y. Kato, S. Ozawa, C. Miyamoto, Y. Maehata, A. Suzuki, T. Maeda, Y. Baba, Acidic extracellular microenvironment and cancer. *Cancer Cell Int.* **13**, 89 (2013).
42. Y.-N. Zhang, W. Poon, A. J. Tavares, I. D. McGilvray, W. C. W. Chan, Nanoparticle-liver interactions: Cellular uptake and hepatobiliary elimination. *J. Control. Release* **240**, 332–348 (2016).
43. M. S. Exton, C. Gierse, B. Meier, M. Mosen, Y. Xie, S. Frede, M. U. Goebel, V. Limmroth, M. Schedlowski, Behaviorally conditioned immunosuppression in the rat is regulated via noradrenaline and beta-adrenoceptors. *J. Neuroimmunol.* **131**, 21–30 (2002).
44. T. M. Buzug, G. Bringout, M. Erbe, K. Grafe, M. Graeser, M. Gruttner, A. Halkola, T. F. Sattel, W. Tenner, H. Wojtczyk, J. Haegele, F. M. Vogt, J. Barkhausen, K. Ludtke-Buzug, Magnetic particle imaging: Introduction to imaging and hardware realization. *Z. Med. Phys.* **22**, 323–334 (2012).
45. I. Giouroudi, E. Hristoforou, Perspective: Magnetoresistive sensors for biomedicine. *J. Appl. Phys.* **124**, 030902 (2018).
46. N. Bertrand, J. Wu, X. Xu, N. Kamaly, O. C. Farokhzad, Cancer nanotechnology: The impact of passive and active targeting in the era of modern cancer biology. *Adv. Drug Deliv. Rev.* **66**, 2–25 (2014).
47. K. T. McVary, A. Razzaq, C. Lee, M. F. Venegas, A. Rademaker, K. E. McKenna, Growth of the rat prostate gland is facilitated by the autonomic nervous system. *Biol. Reprod.* **51**, 99–107 (1994).
48. K. T. McVary, K. E. McKenna, C. Lee, Prostate innervation. *Prostate* **36**, 2–13 (1998).

Acknowledgments: We thank H. Deng, P. Zhang, M. Yin, Z. Ke, X. Wu, Y. Wang, K. Guo, and L. Lu for assistance to finish the experiments. **Funding:** This work was supported by the National Key R&D Program of China under grant no. 2017YFA0205200; the National Natural Science Foundation of China under grant nos. 81671656, 81801668, 81227901, 81527805, and 81501540; the Ministry of Science and Technology of China under grant no. 2017YFA0700401; and the Chinese Academy of Sciences under grant nos. GJJSTD20170004, YJKYYQ20170075, and XDBS01030200. **Author contributions:** H.Y. and W.S. wrote the manuscript, in addition to designing, performing, and analyzing all the experiments. W.S. designed the nanoprobe. H.Y. synthesized and characterized the nanoprobe. X.M. assisted with collecting and analyzing experimental data. J.W., Q.L., and M.L. assisted with the data analysis. L.W. and J.T. conceived the project and supervised and coordinated all the work. **Competing interests:** The authors declare that they have no competing interests. **Data and materials availability:** All data needed to evaluate the conclusions in the paper are present in the paper and/or the Supplementary Materials. Additional data related to this paper may be requested from the authors.

Submitted 7 April 2019
Accepted 22 November 2019
Published 5 February 2020
10.1126/sciadv.aax6040

Citation: H. You, W. Shang, X. Min, J. Weinreb, Q. Li, M. Leapman, L. Wang, J. Tian, Sight and switch off: Nerve density visualization for interventions targeting nerves in prostate cancer. *Sci. Adv.* **6**, eaax6040 (2020).

Downloaded from https://www.science.org on September 09, 2022

ScienceAdvances

Sight and switch off: Nerve density visualization for interventions targeting nerves in prostate cancer

Huijuan YouWenting ShangXiangde MinJeffrey WeinrebQiubai LiMichael LeapmanLiang WangJie Tian

Sci. Adv., 6 (6), eaax6040. • DOI: 10.1126/sciadv.aax6040

View the article online
https://www.science.org/doi/10.1126/sciadv.aax6040
Permissions
https://www.science.org/help/reprints-and-permissions

Downloaded from https://www.science.org on September 09, 2022

Use of this article is subject to the Terms of service

Science Advances (ISSN 2375-2548) is published by the American Association for the Advancement of Science. 1200 New York Avenue NW, Washington, DC 20005. The title *Science Advances* is a registered trademark of AAAS.
Copyright © 2020 The Authors, some rights reserved; exclusive licensee American Association for the Advancement of Science. No claim to original U.S. Government Works. Distributed under a Creative Commons Attribution NonCommercial License 4.0 (CC BY-NC).